Ionics (2006) 12:295–301
DOI 10.1007/s11581-006-0050-2

ORIGINAL PAPER

Nanosized ceria-based ceramics: a comparative study

K. Singh · S. A. Acharya · S. S. Bhoga

Received: 22 August 2006 / Revised: 12 September 2006 / Accepted: 13 September 2006 / Published online: 11 October 2006

Abstract $Ce_{(1-x)}Gd/Sm_xO_{2-\delta}$ (x=0.05–0.2, GDC/SDC) nanometric powder was prepared by glycine-nitrates combustion synthesis, by strictly following uniformity in the preparation route. The thermochemical properties of the obtained precursor were studied by TGA/DTA. Crystallization of the fluorite phase occurred on heating at 800 °C or higher temperature. The grain size of calcined powder was found to be about 15 nm. Densification was studied as a function of dopant content. SDC was found more sinterable than GDC. Crystal structure and microstructure were characterized by means of X-ray diffraction (XRD) and scanning electron microscopy (SEM). Electrical characterization was carried out using the impedance spectroscopy method in the frequency range of 50 Hz–13 MHz. The bulk conductivity of SDC is higher than GDC pellet for all concentration ranges. The results were analyzed by using the concept of change of the chemical bond ionicity due to the replacement of the host by dopant. Guest/host ionic size, valence mismatch ratio and their consequences are counted semi-quantitatively into the configurational and thermal entropy.

Keywords Ceria electrolytes · Combustion synthesis · Electrical conductivity · Bond ionicity · Configurational and thermal entropy

K. Singh
Department of Physics, Amaravati University,
Amaravati, India

S. S. Bhoga
Department of Physics, Nagpur University,
Nagpur, India

S. A. Acharya (✉)
Department of Physics,
Jawaharlal Darda Institute of Engineering and Technology,
Yavatmal-445 001, (M.S.), India
e-mail: saha275@yahoo.com

Introduction

The oxide ion conductor is an important functional material, which can be used as the electrolyte of solid oxide fuel cells (SOFCs), oxygen sensors, and membranes. SOFCs are expected to become the next generation of power systems, having high efficiency and low environmental impact [1]. However, the life of SOFCs is still insufficient for commercial use because of cell degradation under high temperature. At low temperature, it becomes possible to reduce such damage and extend the life of SOFCs. Furthermore, low temperature operation eliminates the need for expensive alloys. However, the ionic conductivity of conventional electrolyte materials, such as Y_2O_3-stabilized-ZrO_2 (YSZ), is not sufficient at low temperature.

To develop a reduced temperature SOFC, various approaches are under consideration. One of these is to use new electrolyte materials that show high ionic conductivity. Ceria-based solid solutions were acknowledged to be the most promising electrolyte for intermediate temperature SOFC (IT-SOFC) since their ionic conductivity is higher than YSZ at the intermediate temperature range (600–800 °C). The ionic conductivity of ceria-based electrolytes doped with various dopants (e.g. Ca^{2+}, Sr^{2+}, Y^{3+}, La^{3+}, Gd^{3+} and Sm^{3+}) at different dopant concentrations was studied [2–7]. Of all these dopants, Gd_2O_3-doped and Sm_2O_3-doped ceria were found to have the highest conductivity [8, 9]. Due to the small association enthalpy between dopant cation and oxygen vacancy in the fluorite lattice [10, 11]. This was confirmed by atomistic computer simulations [12, 13], based on the binding energy between trivalent cations and oxygen vacancies and the corresponding lattice relaxation energy. These simulations suggest that the optimum radius for the trivalent cation in the ceria-based oxide nearly corresponds to the radius of Gd^{3+}, thus supporting the common finding that

gadolinium-doped ceria (GDC) should possess the highest values of ionic conductivity [14]. Yet, other authors reported higher conductivity values for samarium-doped ceria materials [15, 16]. It is thus far from clear whether the properties of GDC exceed those of SDC. Some of the differences between the results reported by different authors were due to factors such as methods of powder preparation and/or sintering schedule [17, 18] due to the variation of grain contribution.

In the present work, $Ce_{(1-x)}Gd/Sm_xO_{2-\delta}$ (x=0.05–0.2) samples were carefully prepared under the identical conditions to minimize differences related to the preparation methods. A combustion synthesis method was used to obtain homogeneous nanocrystalline precursor as described below. Cylindrical pellets, 13 mm in diameter and about 1 mm in height, were obtained by uniaxial pressing at 7 tons/cm^2 for 2 min. The pellets were sintered at varying temperatures (800–1,100 °C) and time (1–6 h). Ionic conductivity was measured by impedance spectroscopy.

Experimental procedure

Gd/Sm-doped CeO_2 powders for different dopant/host ratios were prepared by the glycine-nitrate combustion synthesis. Initial ingredients ($Ce(NO_3)_3{\cdot}6H_2O$) and ($Gd/Sm(NO_3)_3{\cdot}6H_2O$) of GR grade were procured from Aldrich Sigma. The stoichiometric compositions of the redox mixture for combustion were calculated using the concept of propellant chemistry. The detailed procedure is explained in the schematic in Fig. 1. The as-prepared powders were amorphous with some carbon residues. Crystalline and single phase powders were obtained by calcining the powders. The thermal decomposition of the amorphous GDC/SDC presursor was investigated by differential thermal analysis (DTA) and thermo-gravimetric analysis (TGA) between 30 and 1,000 °C with the STA-4000 Netzsch instrument at a heating rate 20 °C/min.

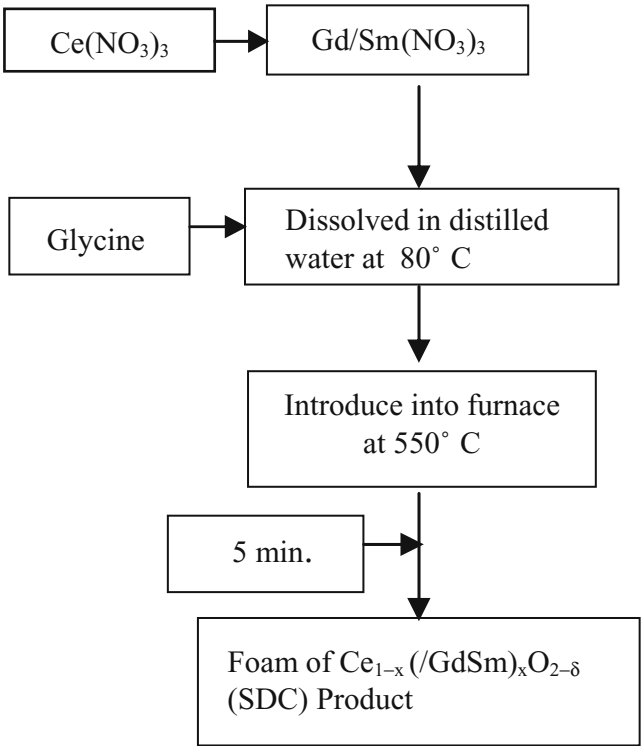

Fig. 1 Flowchart to prepare CeO_2 (doped with Gd/Sm_2O_3) by glycine-nitrate combustion technique

X-ray diffraction analysis (XRD) of the as-sintered samples was performed using the Rigaku D/max-11B X-ray diffractometer with Cu-Kα radiation at a 2θ scan of 1°/min. The reflection from the (111) plane was used for the determination of the average crystallite size. The average crystallite size, D, of the prepared powder was calculated from the Scherrer formula $D=(0.9\lambda/B\cos\theta)$ where λ is the wavelength of the X-rays, θ the diffraction angle, is the corrected half-width of the observed half-width, B_m, of the (111) reflections in samples of SDCx and B_s is the half-width of the (111) reflection in a standard sample of CeO_2.

Green densities of pellets are about 65% of the theoretical. Densities of the sintered pellets were calculated using $\rho=M/V$

$$M = \text{mass of U.C.} = \frac{N[(1-x)M_{Ce} + xM_{Sm} + (2-x/2)M_O]}{N_a}.$$

where V=volume of U.C.=a^3.

The apparent density of each sintered pellet was determined by measuring the diameter and thickness before and after sintering.

$$\text{The relative density in \%} = \frac{\text{Calculated density} - \text{Apparent density}}{\text{Calculated density}} \times 100$$

Microstructures were observed under SEM (XL30, Philips). Grain sizes were measured using the linear intercept method. Ionic conductivities of the sintered pellets were measured over 200–650 °C in air by a two-probe impedance spectroscopy 4192A-impedance analyzer in the frequency range 5 Hz to 13 MHz with sputtered Pt electrodes.

Result and discussion

The TGA/DTA curve for GDC (0.15) and SDC (0.15) are shown in Fig. 2a and b, respectively. In both cases weight loss starts from 50 °C. The rate of weight loss is gradual. The total weight loss is 5–7%. Endothermic peaks are observed at around 250 to 400 °C but are not associated

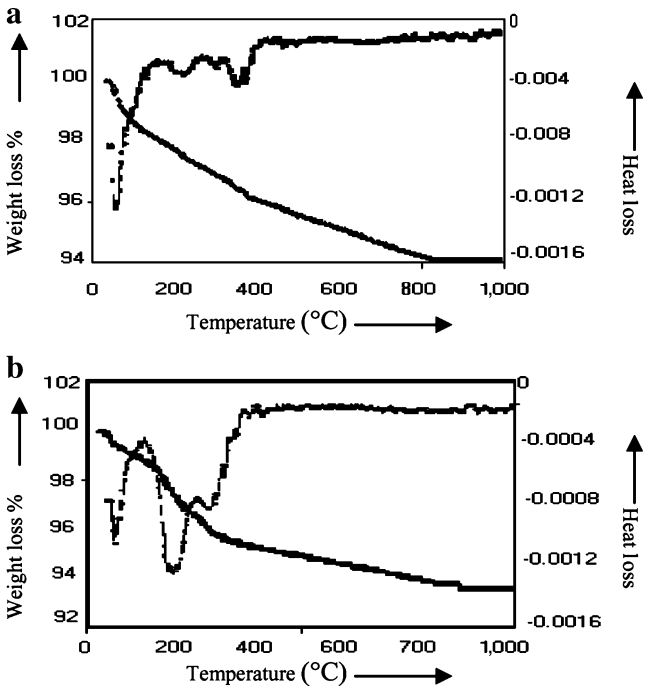

Fig. 2 TGA/DTA of (**a**) GDC and (**b**) SDC powder at dopant concentration x=0.15

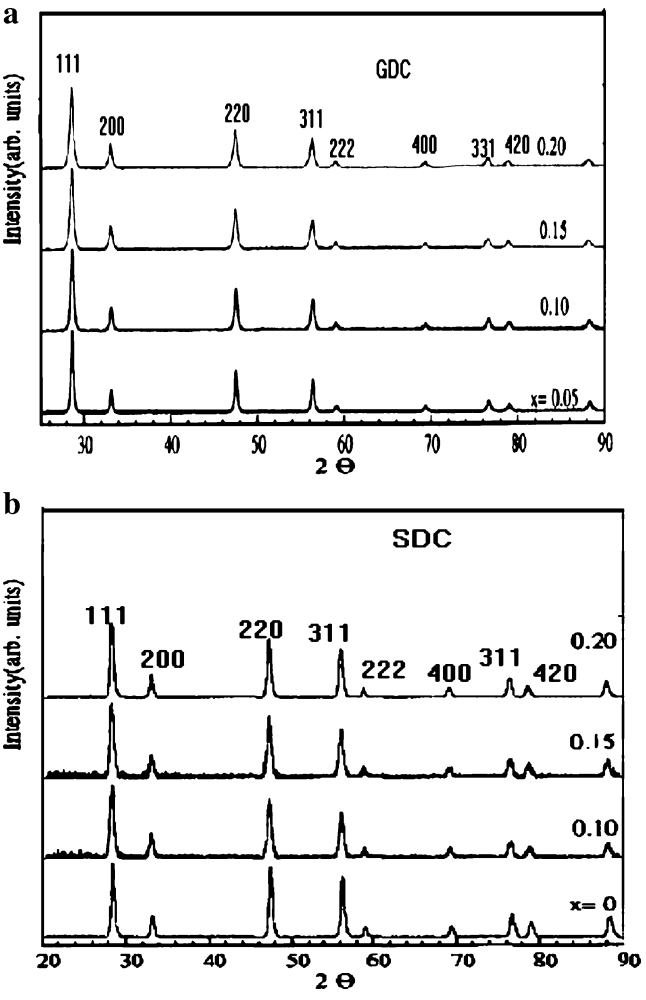

Fig. 3 XRD patterns of the (**a**) GDC (**b**) SDC powders calcined at 800 °C temperature

with any sudden change in mass, can be attributed to the dehydration of water of crystallization. No changes are found in the TGA/DTA curves above 800 °C. This shows that GDC and SDC crystallized almost perfectly at this temperature. No crystalline phases corresponding to Gd_2O_3/Sm_2O_3 are found at any temperature, indicating the direct formation of solid solution. Same trends of the TGA/DTA curves are observed for all samples of this series.

The XRD patterns, shown in Fig. 3a and b indicate that all the compositions used are single phase with a cubic fluorite structure like that of pure CeO_2. The lattice constant was calculated from the XRD pattern by using the relation $a = d\sqrt{(h^2 + k^2 + \ell^2)}$. Figure 4 shows the dependence of 'a', unit cell parameter vs dopant concentration. Unit cell parameter (a) is found to increase with dopant concentration. Wrong size effect, i.e. effect arising in lattice due to the ionic size mismatch of dopant to host, is also observed.

A linear relation between 'a' and 'x' are obtained as: $a(x)$=5.367+0.001x for the GDC series and $a(x)$=5.372+0.0022x for the SDC series.

These results are in good agreement with Vegard's rule.

The average crystallite sizes were calculated by using Scherrer's formula. Table 1 summarizes the lattice parameter, average crystallite size, experimental density, theoretical density and relative density (sintered at 1,100 °C for 6 h) for all samples of GDC and SDC. Samarium shows slightly higher crystallite size than gadolinium. Crystallite size is not much affected by the content of the dopants.

To study the comparative sinterability of GDC and SDC, a comparison is drawn between dopant content and relative density of GDC and SDC at a temperature of 1,100 °C for a holding time of 6 h (Fig. 5). Pure CeO_2

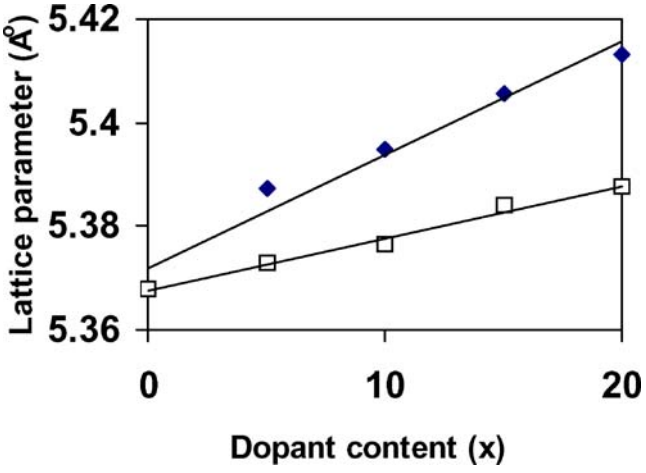

Fig. 4 Lattice constant of (*open square*) GDC and (*closed diamond*) SDC at dopant concentration (0–20 mol%)

Table 1 The lattice parameter, average crystallite size, experimental density, theoretical density and relative density (sintered at 1,100 °C for 6 h) for Gd/Sm-doped ceria

Sample	Lattice parameter (Å)	Average crystallite size (nm)	Calculated density (kg/V^3)	Apparent density (kg/V^3)	Relative density (%)
CeO_2	5.3679	10.40	7.3903	6.6513	91
GDC0595	5.3728	6.87	7.3896	6.7245	92
GDC1090	5.3764	6.87	7.3943	6.8027	93
GDC1585	5.3839	6.87	7.3828	6.9398	95
GDC2080	5.3875	12.95	7.3874	6.9959	95.7
SDC0595	5.3874	12.96	7.3151	6.7298	93
SDC1090	5.3947	12.95	7.2903	6.7799	94
SDC1585	5.4057	12.94	7.2507	6.8881	96
SDC2080	5.4132	6.86	7.2254	6.9002	96.5

exhibits a lower density than doped ceria. This suggests that dopants (Gd/Sm) accelerate densification of CeO_2. Relative density (RD) as a function of dopant content shows (Fig. 5) that RD increases with dopant content, as already explained in our earlier work [19]. Same trends are observed for both dopants.

Even though the particles' size of GDC is smaller than SDC (calculated by XRD), SDC is found more sinterable than GDC. This indicates that in nanometric solid solution, for densification process, bulk changes are dominated by localized modification. So localized effective parameters like ionic size, bonding between cation to anion and their role in the process must be considered for comprehensive understanding of sinterability. The ionic bond strengths are calculated by using Pauling's equation based on the average electronegativities of cation and anion. The equation can be expressed as

$$P_{AB} = 1 - \exp\left[-\frac{1}{4}(x_A - x_B)\right] \quad (1)$$

where P_{AB} is the ionic bond strength, x is the average electronegativity, and the subcripts A and B are cations and anions, respectively. Table 2 reveals that (1) the ionic size of samarium is larger than gadolinium and cerium, (2) the ionic bond strength of Sm–O is larger than Gd–O and smaller than Ce–O, and both conditions are favourable to samarium for thermal expansion at the localized level, which in turn attributes to the increase in packing density at bulk level. This facilitates that the samarium-doped system is more sinterable than gadolinium-doped. In almost all samples, relative packing density above 95% is attained at 1,100 °C for 5–6 h sintering.

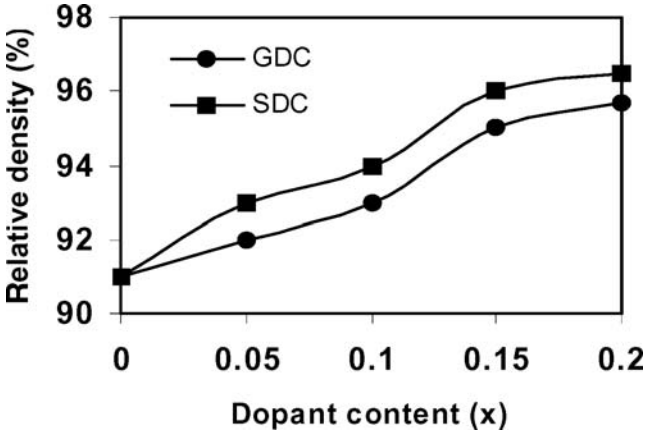

Fig. 5 Dopant content dependence of relative density for $Ce_{1-x}Sm/Gd_xO_{2-\delta}$ ceramics at 1,100 °C for 6 h

A typical microstructure of GDC1585 and SDC1585 are shown in Fig 6a–d. The surface view of the micrograph of GDC and SDC pellets sintered at 1,000 °C for 6 h (Fig. 6a and c), shows non-agglomerated well-developed grains with high porosity. The average grain size is about 100 nm. Figure 6b and d depicts the microstructure of the pellets sintered at 1,100 °C for 6 h. The surface micrograph observation of the sintered pellets indicates highly dense structure with formation of well-defined grain separated by grain boundary. The grain growth is in sub-micrometer range. A careful look of the micrograph (Figs. 6b and d) reveals that grains are non-uniform in size and shape, and there is no evidence of exaggerated grain growth, however size difference between smaller and larger grains are more in GDC than SDC.

Figure 7a and b shows the comparative cole–cole plots of impedance for GDC and SDC for dopant concentration x=0.05 and x=0.15, respectively at a temperature of 350 °C. The data fall on a single semicircle whose center lies below the real axis at high frequencies indicating the non-Debye nature of the material. The associated capacitance of the

Table 2 Ionic radii, electronegativity and ionicity of cation–O bond in doped ceria

Sample	Ionic radii (Å)	Electronegativity	Ionicity cation–O
CeO_2	0.92	1.12	Ce–O=0.738
GDC	0.938	1.21	Gd–O=0.712
SDC	0.964	1.17	Sm–O=0.722

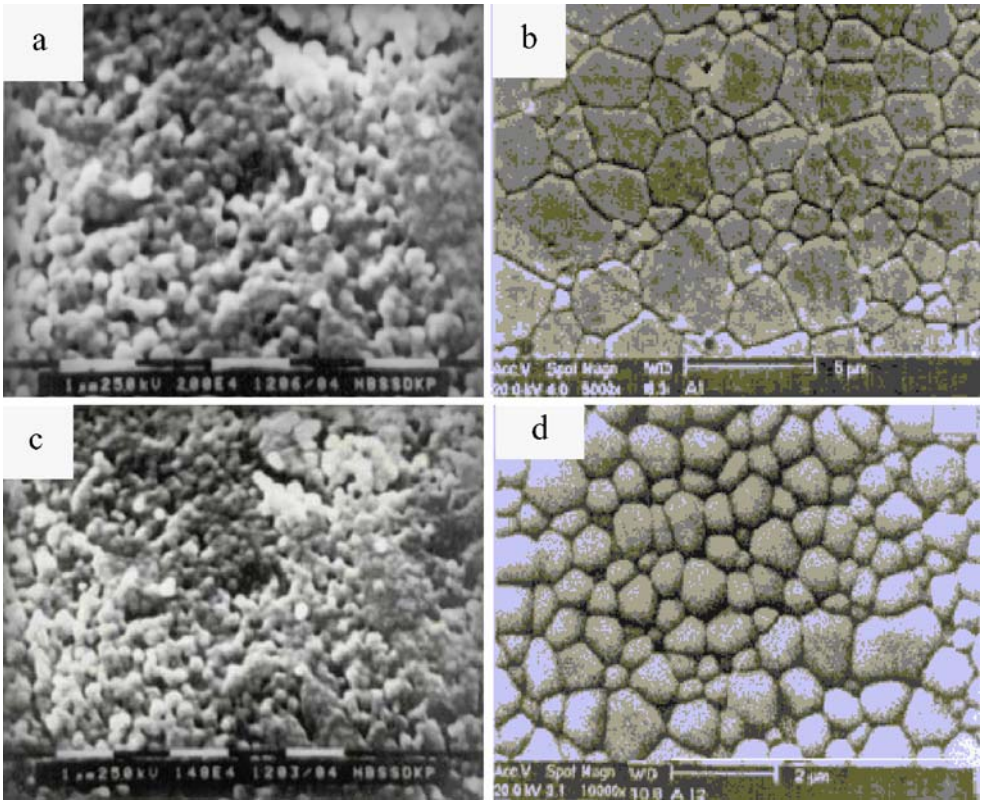

Fig. 6 SEM of 6 h sintered pellets of GDC1585 at (**a**) 1,000 °C, (**b**) 1,100 °C, and SDC1585 (**c**) 1,000 °C and (**d**) 1,100 °C

semicircle was calculated from the relation ωrc=1 at the arc maximum and it is found to be in the order of pF that is attributed to a conduction process through the bulk of the materials [20]. The bulk resistance of the samples at various temperatures was calculated from the low frequency intercepts of the real axis. The bulk resistance of the SDC series are found to be low compared to GDC series for all temperatures. The bulk resistance is found to be decreasing with increasing temperature for both the series. The bulk resistance value of both the samples indicates that SDC have high ionic conductivity than GDC for all dopant concentrations.

The bulk conductivity is chiefly governed by the ionic size and the valence of the guest substituting cation [21]. In our case, SDC and GDC systems, both guests Gd^{3+}/Sm^{3+}, are larger in size than Ce^{4+}. The partial replacement of the host by the guest creates additional oxygen vacancies and forces the lattice to expand in the vicinity of the guest ion. Such local lattice expansion results into a rise of the entropy and the enthalpy. The disorder reaction can be written using Kröger–Vink notation as

$$(1-x)CeO_2 + (x)Gd_2O_3 = (1-x)Ce_{Ce}(CeO_2) + (x)\left[Gd'_{Ce}(CeO_2) + V'_O(CeO_2)\right] \quad (2)$$

The defect reaction for Sm^{3+}-doped CeO_2 would be similar. To maintain the thermodynamic stability, local electroneutrality and constancy in chemical potential, the reaction (2) follows

$$n = (k_f)^{1/2} \exp\left[\frac{\Delta S_{th} + \Delta S_{cf}}{k}\right] \exp\left[\frac{-E_f}{kT}\right] \quad (3)$$

where n, ΔS_{th}, ΔS_{cf} and E_f are the defect concentration, thermal entropy, configurational entropy and defect formation enthalpy, respectively.

Since both the Gd^{3+} and Sm^{3+} guests are (Table 2) larger in size than the host Ce^{4+}, the partial replacement of the latter by the former not only creates additional oxygen vacancies but also forces the lattice to expand in the vicinity of the guest ion (i.e., opens the bottleneck). Subsequently, the lattice near the guest $(Gd/Sm)^{3+}$ undergoes a local strain up to a few atomic distances. Such local lattice expansion results into the rise of the entropy and the enthalpy.

The system under consideration is assumed to be uniform, homogeneous, and isotropic. The configurational entropy, ΔS_{cf}, of such a crystal is given by

$$\Delta S_{cf} = k \log(W_{cf}) = k \log\left|\frac{N_a + N_c}{N_a!\, N_c!}\right| \quad (4)$$

where w_{cf} represents the number of all probable different arrangements of mobile N_a anions and N_c cations distributed

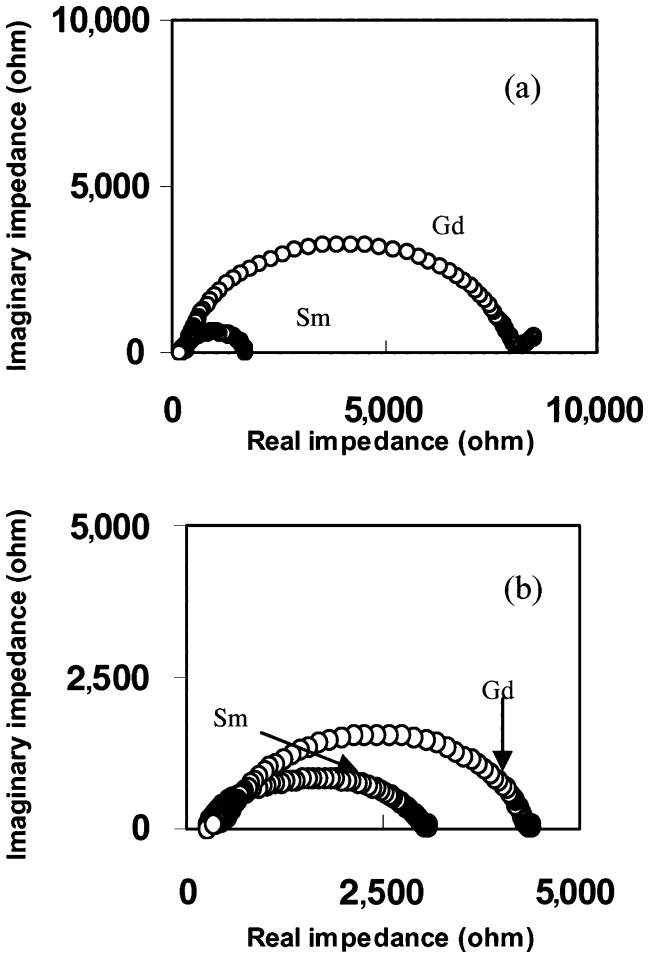

Fig. 7 Comparative impedance spectra of GDC and SDC at 350 °C (**a**) x=0.05, (**b**) x=0.15

over a total of (N=N_a+N_c) lattice sites. Since in the present case tetravalent Ce^{4+} is replaced by trivalent $(Gd/Sm)^{3+}$, the distribution of N_c with respect to N_a over all available lattice sites does change, whereby, varies ΔS_{cf}. Practically, after doping, the number of ions available to occupy the regular lattice cites is more than the number of available sites. Concurrently, additional anion vacancies are created leading to an increase in configurational enthalpy as per the relation Eq. (4). At the same time, the ions neighboring the impurity $(Gd/Sm)^{3+}$ would have a vibrational frequency ν' smaller than that for those at regular undistorted sites ν as a result of reduced restoring forces. To simplify the discussion, here we shall assume that in the doped crystal, each ion neighbouring a $(Gd/Sm)^{3+}$ is, in the Einstein model, equivalent to three harmonic oscillators of a frequency $\nu'<\nu$. Thus for a single ion, the number of nearest mobile ions surrounding $(Gd/Sm)^{3+}$, the Einstein model leads to: X_A oscillators of frequency ν'; $3N-X_A$ oscillators of frequency ν where 'X_A'=xN_A. Here, x is the mol% of dopant $(Gd/Sm)_2O_3$ and N_A is Avogadro's number. The change in thermal entropy per guest ion is given by

$$\Delta S_{th} = \left[X_A k\left(1+\log\left(\frac{kT}{h\nu'}\right)\right)+(3N-X_A)k\left(1+\log\left(\frac{kT}{h\nu}\right)\right)\right] - \left[3Nk\left(1+\log\left(\frac{kT}{h\nu}\right)\right)\right] \quad (5)$$

The first and the second terms are due to doped and perfect crystals, respectively. i.e.,

$$\Delta S_{th} = k\ \log\ (\nu/\nu') \quad (6)$$

Although the employed model is a very simplified one, it demonstrates the fact that ΔS_{cf} and ΔS_{th} are the consequences of change in the effective number of ions and the frequency of the lattice vibration due to its expansion, respectively. Taking into consideration the validity of this model, the defect concentration can be expressed by

$$n = (k_f)^{1/2}\left[(\nu/\nu')\exp\ \left[-E_{f/kT}\right]\right. \quad (7)$$

Since $\nu>\nu'$, the change in thermal entropy due to $(Gd/Sm)^{3+}$ addition favours the defect formation.

The lattice distortion not only changes entropy but also modifies the mutual Coulombic interaction between the cation under consideration and its nearest neighbouring ions. The local lattice expansion increases the distance between $(Gd/Sm)^{3+}$ and O^{2-}, and the nearest alike ions, thereby, the reduction in interaction energy. The interaction energy according to Born [22] and Madelung [23] can be written as

$$E = \left(-X_A 4e^2\right)/r \quad (8)$$

Thus, the increase in inter-ionic distance, r, due to lattice expansion, reduces activation energy.

Although the energies, in general, cannot be represented accurately by Eqs. (7) and (8), the above treatment provides some useful approximate semiquantitative conclusions, which are helpful in understanding the fundamental conduction mechanism.

Conclusion

A combustion synthesis method is suitable to prepare nanometric powders of ceria-based materials. The as-prepared powders are amorphous but the fluorite phase is readily formed by heating at 800 °C. These powders were used to prepare ceramic samples of gadolinium-doped ceria and samarium-doped ceria. Strict uniformity in the preparation conditions was maintained. The XRD analysis reveals the nanocrystalline phase of both samples. Relatively low temperature is needed to densify the samples

prepared by this method. Sm-doped samples were found to have higher sinterability compared to Gd-doped samples. The impedance analysis reveals that the Sm-doped ceria has high ionic conductivity compared to Gd-doped ceria. The results were analyzed by using the concept of change of the chemical bond ionicity due to the replacement of the host by dopant. Guest/host ionic size, valence mismatch ratio and their consequences are counted semiquantitatively into configurational and thermal entropy.

References

1. Minh NQ (2004) Solid State Ion 174:271
2. Wang DY, Park PS, Griffith J, Nowick AS (1981) Solid State Ion 2:95
3. Blumenthal RN, Brugner FS, Garnier JE (1973) J Electrochem Soc 120:1230
4. Yahiro H, Eguchi K, Arai H (1986) Solid State Ion 21:37
5. Faber J, Geoffroy C, Roux A, Sylvestre A, Ablard P (1989) Appl Phys A 49:225
6. Balaza GB, Glass RS (1995) Solid State Ion 76:155
7. Zhang TS, Hing P, Huang HT, Kilner JA (2002) Solid State Ion 148:567
8. Yahiro H, Eguchi Y, Eguchi K, Arai H (1988) J Appl Electrochem 18:527
9. Steele BCH (1989) In: T. Takahashi (ed.) High conductivity solid ionic conductors, recent trends and applications, World Scientific London, p 402
10. Anderson R Gerhard, Nowick AS (1981) Solid State Ion 5:547
11. Kilner JA (1983) Solid State Ion 8:201
12. Minervini L, Zacate MO, Grimes RW (1999) Solid State Ion 116:339
13. Hayashi H, Sagawa R, Inaba H, Kawamura K (2000) Solid State Ion 131:281–290
14. Steele BCH (2000) Solid State Ion 129:95
15. Yahiro H, Eguchi K, Arai H (1989) Solid State Ion 36:71
16. Inaba H, Tagawa H (1996) Solid State Ion 83:1
17. Riess I, Braunsbtein D, Tannhauser DS (1981) J Am Ceram Soc 64:480
18. Adham KE, Hammou A (1983) Solid State Ion 9–10:905
19. Singh K, Acharya SA, Bhoga SS (2006) Mater Chem Phys (communicated on May 27, 2006)
20. Bhuvaneswari MS, Selvasekarapandian S, Vijay-kumar M, Hirankumar G (2004) J Mater Sci 39:727–729
21. Singh K, Pande SM, Bhoga SS (1995) J Solid State Chem 116:232
22. Born M (1933) Handbuch der Physik, vol 24/2. Springer, Berlin Heidelberg New York
23. Madelung E (1910) Phys Z Sowjetunion 11:898